Chapter 10
Dip Coating

C. Jeffrey Brinker

10.1 Introduction

Among the various wet chemical thin film deposition methods dip coating represents the oldest commercially applied coating process. The first patent based on this process was issued to Jenaer Glaswerk Schott & Gen. in 1939 for sol-gel derived silica films [1]. Nowadays sol-gel [2] or more general CSD derived coatings are being studied for a manifold range of applications such as ferroelectrics, dielectrics, sensors and actuators, membranes, superconducting layers, protective coatings, passivation layers, etc. (see Part V of this book). Basically the process may be separated into three important technical stages:

1. Immersion & dwell time: The substrate is immersed into the precursor solution at a constant speed followed by a certain dwell time in order to leave sufficient interaction time of the substrate with the coating solution for complete wetting.
2. Deposition & Drainage: By pulling the substrate upward at a constant speed a thin layer of precursor solution is entrained, i.e. film deposition. Excess liquid will drain from the surface.
3. Evaporation: The solvent evaporates from the fluid, forming the as-deposited thin film, which can be promoted by heated drying. Subsequently the coating may be subjected to further heat treatment in order to burn out residual organics and induce crystallization of the functional oxides.

At first glance this coating method is rather simple, however a more detailed understanding of the microscopic processes during dip coating enables tailoring of the final films since it is the coating process that serves as one important link between the structure of the solution or sol, respectively, and the microstructure of the deposited film. Hence this chapter addresses the fundamentals of the underlying

C.J. Brinker (✉)
Sandia National Laboratories, Albuquerque, NM 87185, USA
e-mail: cjbrink@sandia.gov

T. Schneller et al. (eds.), *Chemical Solution Deposition of Functional Oxide Thin Films*,
DOI 10.1007/978-3-211-99311-8_10,

physics and chemistry of the thin film formation by dip coating including recent findings. Although the dip coating process can be applied to all types of precursor solutions (sol-gel, MOD and hybrid, compare Chap. 3 the use of sol-gel type solutions offers the most possibilities to influence the film properties by modifying the size and structure of the inorganic species in the sol together with the solvent(s). Thus though already mentioned in other chapters of this book briefly the corresponding aspects of sol-gel chemistry are reviewed at first. Then the features of the classical dip coating process are discussed by means of sol-gel derived coatings. This comprises the deposition of inorganic sols with regard to time scales and the effects of sol structure and capillary pressure on such properties as refractive index, surface area, and pore size of the deposited film. Finally advanced dip coating approaches like angular dependent dip coating and the evaporation-induced self-assembly (EISA-process), which enable the rapid production of patterned porous or nanocomposite thin film materials, are presented.

10.2 Precursor Solution Chemistry

At first some general comments to the requirements of precursor solutions with regard to successful dip coating are presented in this section. A trivial but probably most important precondition is that the condensed phase remain dispersed in the fluid medium, that macroscopic gelation be avoided, and that the sol be sufficiently dilute so that upon deposition the critical cracking thickness not be exceeded (see discussion in Sect. 10.3.3). Thus in principle all different kinds of sols or solutions described in Part I of this book can be used for dip coating, although as will be shown in the following sections, the differences in the structures of the condensed phase lead to differences in the structures of the deposited films. Since sol-gel type precursor solutions offer the most obvious opportunities to influence these structures of the condensed phase during the coating process, some basics of sol-gel chemistry are briefly reviewed at this point.

In general the sol-gel process uses inorganic or metallo-organic precursors [2]. In aqueous or organic solvents, the precursors are hydrolyzed and condensed to form inorganic polymers composed of M-O-M bonds. For inorganic precursors (salts), hydrolysis proceeds by the removal of a proton from an aquo ion $[M(OH_2)_n]^{z+}$ to form a hydroxo (-OH) or oxo (=O) ligands. Condensation reactions involving hydroxo ligands result in the formation of bridging hydroxyl (M-μ(OH)-M) or oxo (M-O-M) bonds. Normally, monomeric aqueous ions are the only stable species at low pH and various monomeric or oligomeric anions the only species observed at high pH. At intermediate pH, well-defined polynuclear ions are often the stable solution species, but the metal solubility is normally limited there and, when exceeded, results in the precipitation of oxyhydroxides or oxides [3]. The most commonly used molecules are metal alkoxides which are described in more detail in Chap. 1 in this book. Often the alkoxide is dissolved in its parent alcohol and hydrolyzed by the addition of water plus, in the case of more electronegative metals

or metalloids, acid or base catalyst. Hydrolysis replaces alkoxide ligands with hydroxyl ligands. Subsequent condensation reactions involving the hydroxyl ligands produce oligomers or polymers composed of M-O-M or M-μ(OH)-M bonds.

For both inorganic and metallo-organic precursors, the structure of the evolving oligomers or polymers depends on the extent of hydrolysis and the preferred coordination number or functionality of the metal [2, 4].

In the case of inorganic precursors, the extent of hydrolysis is generally controlled by the pH (cp. also Chap. 14), while the effective functionality may be controlled (reduced) through complexation with mono- or multidentate anionic species. The extent of hydrolysis of metallo-organic precursors is controlled through the molar ratio (r) H_2O/M and the catalyst concentration. Since many of the metals of interest for functional oxide thin films (e.g. Al, Ti, Zr, Nb, Ta etc.) have coordination numbers (CN) $\geq$4, complete condensation would lead to compact, particulate metal oxides. In order to avoid this, chemical modification of the metal alkoxide with chelating or bridging multidentate ligands is generally used to reduce both the effective functionality and the overall extent of condensation [4]. NMR, SAXS, and diffraction studies have documented that the above strategies allow the structure of the condensed species to be varied over a wide range spanning monomers, oligomers, polymers, and nanocrystals [2]. Often so-called "polymeric sols" are characterized by a mass or surface fractal dimension (see discussion in Sect. 10.3.4).

By using humidity insensitive MOD-type precursor solutions unintended hydrolysis&condensation reactions can be avoided. However in this case the microstructure directing influence of the classical sol-gel reaction is lost.

10.3 Classical Dip Coating

In the standard approach, the substrate is withdrawn vertically from the solution reservoir at a constant speed U_0 (Fig. 10.1) [5]. According to the streamlines in Fig. 10.1 the moving substrate entrains the liquid in a fluid mechanical boundary layer that splits in two above the liquid bath surface, returning the outer layer to the bath [6].

Above the stagnation point S (Fig. 10.1), when the upward moving flux is balanced due to evaporation, the film position and shape of the film profile remain steady with respect to the coating bath surface. Since the solvent is evaporating and draining, the entrained film acquires an approximate wedge-like shape that terminates in a well-defined drying line (x = 0 in Fig. 10.2). Above this vapor-liquid-solid three-phase boundary (drying line) the non-volatile species form the as-deposited layer which may be subjected to further curing. Figure 10.2 shows schematically the microscopic processes which occur within the thinning film. The

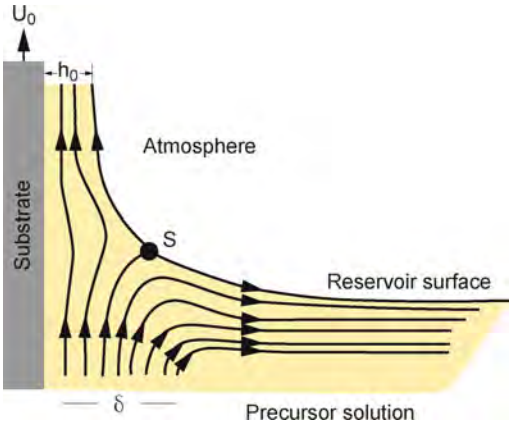

Fig. 10.1 Detail of the flow patterns (streamlines) during the dip-coating process. U_0 is the withdrawal speed, S is the stagnation point, δ the boundary layer, and h_0 is the thickness of the entrained fluid film on the substrate

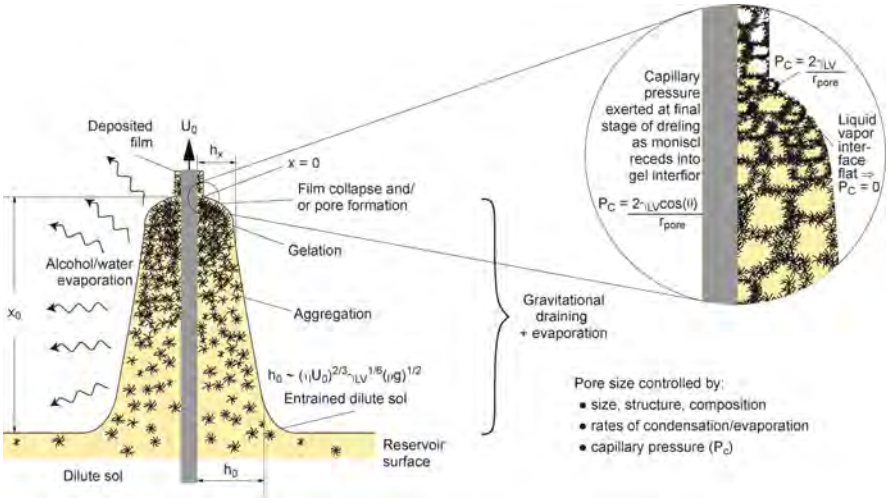

Fig. 10.2 Schematic of the steady-state dip-coating process, showing the sequential stages of structural development that result from draining accompanied by solvent evaporation and continued condensation reactions. U_0 is the withdrawal speed; *h(x)* is the film thickness at position x measured from the drying line $x = 0$; h_0 is the entrained film thickness just above the stagnation point S, i.e. before evaporation; η is the liquid viscosity; ρ is the liquid density; P_C is the capillary pressure; γ_{LV} is the liquid-vapor surface tension; r_{pore} is the pore size and θ is the wetting angle

inorganic species are progressively concentrated by evaporation, leading to aggregation, gelation, and final drying to form a type of dry gel or *xerogel layer*.

In order to model the thickness evolution during dip-coating several regimes have been taken into account. According to Scriven [6] the entrained thickness h_0

(see Fig. 10.2) of the deposited film is related to the streamline dividing the upward and downward moving layers (Fig. 10.1). In principle a competition between various forces in the film deposition region governs the film thickness and the position of the stream line [6].

- When the liquid viscosity η and withdrawal speed U_0 are high enough to lower the curvature of the gravitational meniscus, the deposited film thickness h_0 is that which balances the viscous drag (ηU_0) and gravity force (ρg) [6, 7] according to:

$$h_0 = c_1(\eta U_0/\rho g)^{1/2} \tag{10.1}$$

where ρ is the liquid density, g is the acceleration of gravity and the constant c_1 is about 0.8 for newtonian liquids.

- When the substrate speed (typical range of ~1–10 mm/s) and liquid viscosity η are low, as is often the case for sol-gel film deposition, this balance (Eq. 10.1) is modulated by the ratio of viscous drag to liquid-vapor surface tension γ_{LV}, according to the relationship derived by Landau and Levich for a newtonian and non-evaporating fluid [7]:

$$h_0 = 0.94\frac{(\eta U_0)^{2/3}}{\gamma_{LV}^{1/6}(\rho g)^{1/2}} \tag{10.2}$$

At usually applied withdrawal speeds in the range of ~1–10 mm/s this draining approach often describes the thickness evolution of dip-coating derived films relatively well, however recently the group of Grosso [8, 9] showed by means of various silicon-/titanium oxide precursor solutions, that in case of ultra-slow withdrawal speeds, i.e. below 0.1 mm/s or other extreme conditions such as high evaporation rate, highly reactive species in the precursor solution etc., this model cannot describe the coating results. In order to explain the finding that the (final) thickness vs. withdrawal speed curve (Fig. 10.3a) shows a minimum, the "capillarity regime" was introduced and modeled by semiexperimental equations.

- In case of very low withdrawal speeds, i.e. in the capillarity regime, the solvent evaporation becomes faster than the movement of the drying line leading to a continuous feeding of the upper part of the meniscus by the precursor solution through capillary rise (Fig. 10.3b).

  By assuming that the evaporation rate E is constant and applying the mass conservation law the following relation for the final film thickness h_f (i.e. after stabilization by thermal treatment) could be derived for the capillarity regime [9]:

$$h_f = \frac{c_i M_i E}{\alpha_i \rho_i L U_0} = k_i\left(\frac{E}{LU_0}\right) \tag{10.3}$$

where c_i is the inorganic precursor solution concentration, M_i is the molar weight of inorganic material, α_i is the fraction of inorganic material in the film [9], ρ_ι is the density of the inorganic material, and L is the width of the film. Since α_i does not vary significantly with U_0 a new solution dependent material proportion constant k_i

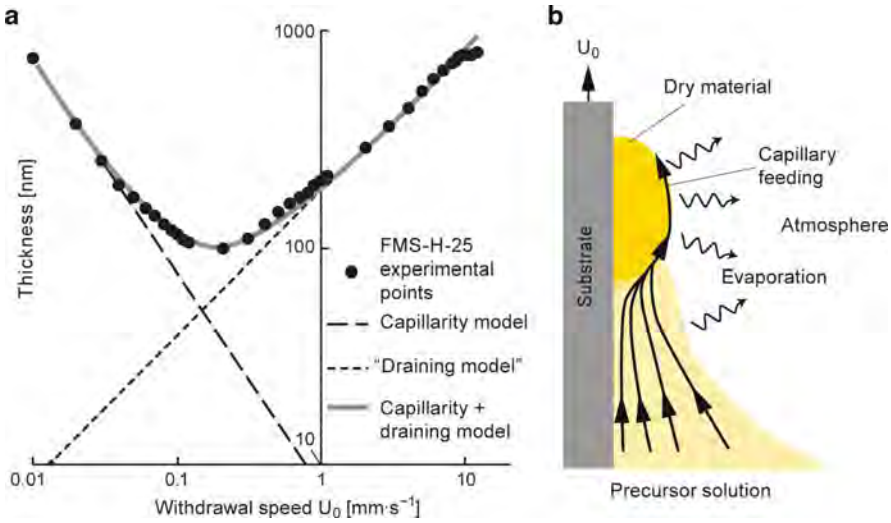

Fig. 10.3 (**a**) Plot of the final thickness (h_f) versus withdrawal speed (log-log scale) for a precursor solution system consisting of tetraethylorthosilicate, methyltriethylorthosilicate and the block copolymer Pluronic® F 127 in ethanol (FMSi-H-25)—experimental points and corresponding models for both independent (*dashed line*) and combined (*solid line*) capillarity and draining regimes of film formation (modified after [9]). (**b**) Schematic illustration of the dip coating process in case of the capillarity regime

is introduced. Equation (10.3) describes relatively well the (final) thickness in case of withdrawal speeds of 0.01 mm/s to ~0.1 mm/s are applied.

- In order to model the intermediate U_0 values (~0.1 and 1 mm/s), where the $h_f(U_0)$ curve exhibits a minimum (Fig. 10.3a), it was taken into account that both regimes ("draining" and "capillarity") are overlapping. Before summing up both contributions at first a relation for the final thickness h_f in case of the draining regime (Landau-Levich model) was derived from Eq. (10.2) considering the evaporation by introducing the material proportion constant k_i into the equation. The physicochemical constants of the precursor solution are combined to a global constant D leading to Eq. (10.4) which now describes the final film thickness, disregarding any evaporation-dependent parameters, such as viscosity, surface tension and possible condensation in sol-gel type precursors.

$$hf = k_i D {U_0}^{2/3} \tag{10.4}$$

Since k_i and h_0 were known for each speed U_0, D was calculated from experimental data and found to be roughly constant if U_0 was in the typical range of 1 to ~10 mm/s, which is a requirement for the Landau-Levich based model. Only a slight decrease of D is found for the highest values of U_0 [9] which was attributed to the fact that under these conditions the thickness of the deposited solution is too high for the gravity-induced viscous drag to be

counterbalanced by the adhesion of the layer to the surface [10]. Hence summing up Eqs. (10.3) and (10.4) yields Eq. (10.5) which describes the experimentally measured thickness evolution of a number of dip coated sol-gel type precursor solutions quite well (Fig. 10.3) [9].

$$hf = k_i \left(\frac{E}{LU_0} + DU_0^{\,2/3} \right) \tag{10.5}$$

From setting the derivative (dh_f/dU_0) of Eq. (10.5) to zero the intermediate critical speed $U_{0,C}$ at the minimum thickness $h_{f,min}$ can be calculated by Eq. (10.6).

$$U_{0,C} = \left(\frac{2DL}{3E} \right)^{-\frac{3}{5}} \tag{10.6}$$

Although this semiexperimental approach cannot describe time dependent parameters like viscosity variation, evaporation cooling, thermal Marangoni flow etc., the calculated values for the critical speed and minimum thickness for a number of precursor systems was in good agreement with experimental data [9]. The observed tendency to two opposite film thickness evolution regimes enables a good control of the thickness (from very thin to ultrathick) by using the same precursor solution. Thereby the speed of deposition in the capillary regime can be considerably increased by using warm air because it is governed by the evaporation rate E.

10.3.1 Pure and Binary Fluids

Although the classical expression (10.2) was developed for pure fluids (i.e. those with no condensed phase), several studies of sol-gel dip coating have verified the $h_0 \sim U_0^{2/3}$ relationship predicted by Eq. (10.2) (e.g., [11]), suggesting that the entrainment of inorganic species has little effect on the hydrodynamics of dip coating, at least at the early stages of deposition where the entrained sol is quite dilute. Some insight into the sol-gel film deposition was revealed by "imaging ellipsometry" [12] and "fluorescence imaging" [13, 14] of the steady state film profile (Fig. 10.2). Thereby imaging ellipsometry allowed the in situ determination of film thickness h and film refractive index n over the complete film profile, while embedded organic dyes acted as molecular sensors of the progressively changing physical and chemical environments created within the thinning film.

Whereas the entrained film thickness immediately above the stagnation point depends on hydrodynamic factors, the shape of the film profile $h(x)$ in the vicinity of the drying line is established by the evaporation rate. Hurd showed that for a planar substrate geometry, the evaporation rate E of a pure fluid was not constant but diverged at the drying line ($x = 0$ in Fig. 10.2) according to expression (10.7) [15]:

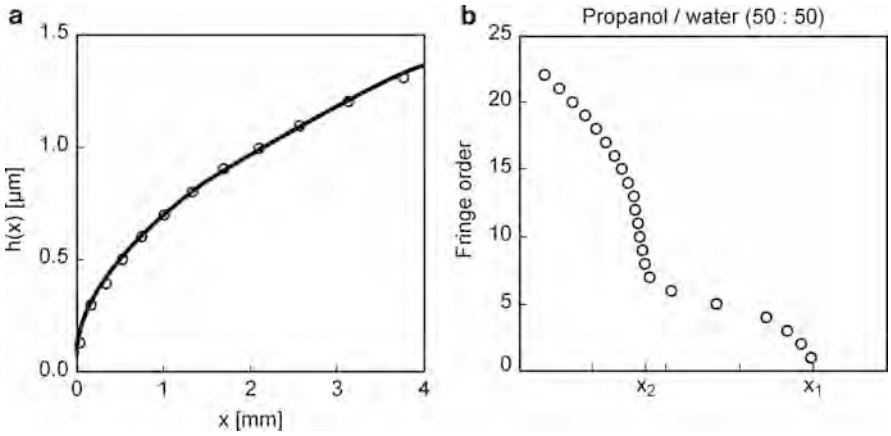

Fig. 10.4 Thickness profiles two of dip coated films from different solutions. (**a**) Ethanol film (*circles*) where the profile can be fitted quite well by Eq. (10.8) (*solid line*). (**b**) Double parabolic profile of a 50:50 propanol:water film (volume ratio) caused by differential volatilities and surface tension gradient driven flows. x_1 is the position of the drying line; x_2 is the position of the "false" drying line created by the depletion of the propanol-rich phase. The film thickness equals approximately the fringe order times 240 nm. Modified after [15, 16]

$$E(x) = D_v a x^{-1/2} \tag{10.7}$$

where D_v is the diffusion coefficient of the vapor, and a is a constant.

The divergence of the evaporation rate causes the film to thin more quickly in the vicinity of the drying line, so instead of exhibiting a wedge-shape (the expectation for uniform evaporation) the film profile acquires a parabolic shape (Fig. 10.4a):

$$h(x) \sim \int E(x)dx \sim x^{1/2} \tag{10.8}$$

For multicomponent fluids (e.g., alcohol/water mixtures often used in alkoxide-based sols) differences in the evaporation rate's and surface tensions of the individual fluid components alter the shape of the film profile and create convective flows within the depositing film. For example, for binary alcohol/water mixtures, the film profile shows two roughly parabolic regions (see Fig. 10.4b). The first corresponds to the preferential evaporation of alcohol to leave a water-rich fluid. The difference in surface tensions between the water-rich and alcohol-rich regions induces liquid flow into the water-rich "foot" with velocity u the so-called "Marangoni effect" [5, 11]:

$$u = \frac{1}{\eta}\left[\frac{d\gamma}{dx}\right] z - U_0 \tag{10.9}$$

where z is the direction normal to the substrate surface (i.e. $z = h$). The foot slowly grows until this flux is balanced by that of evaporation from the expanding free

surface. There are several consequences of preferential evaporation and surface tension gradient driven flows with respect to sol-gel film deposition:

- It is the composition of the fluid that persists to the drying line that establishes the surface tension and hence the magnitude of the capillary pressure exerted on the condensed phase (Fig. 10.2). Fluorescence imaging performed by Nishida and co-workers [13] has shown that for ethanol/water/silica sols, the composition of the fluid at x = 0 is greater than 80 % water, when the initial sol contains only 12.5 volume % water.
- The surface tension gradient-driven flow of liquid through a thin "neck" can create quite high shear rates during dip-coating. For the toluene:methanol (50:50) system, the shear rate resulting from surface tension gradient driven flow is estimated to be 10^4 s^{-1} [15]. Such shears could be sufficiently strong to align or order the entrained inorganic species.

10.3.2 Effect of Condensed Phases

The previous sub-sections have largely ignored the effects of the entrained inorganic species, viz., polymers or particles. These species are initially concentrated by evaporation of solvent(s) as they are transported from the coating reservoir toward the drying line within the thinning fluid film during withdrawal. They are further concentrated (compacted) at the final stage of the deposition process by the capillary pressure P_C (Fig. 10.2). In the following paragraphs the various factors are discussed.

10.3.2.1 Solids Concentration and Time Scale

Above the stagnation point (see Fig.10.1) all fluid elements are moving upward, which means that all the entrained inorganic species that survive past the stagnation point are incorporated in the final deposited film. Steady state conditions in this region require conservation of non-volatile mass, thus the solids mass in any horizontal slice (dm_i in Fig. 10.5a) of the thinning film must be constant [16]:

$$h(x)\phi(x) = constant \tag{10.10}$$

where $\phi(x)$ is the concentration, or volume fraction solids, respectively. From Eq. (10.10) it can be seen that ϕ varies inversely with h, if $h << h_0$ (the normal case for sol-gel dip-coating). In case of planar substrates which have a parabolic thickness profile ($h(x) \approx x^{1/2}$) [6], ϕ should vary as $1/h \approx x^{-1/2}$ in the thinning film [15].

The rapid concentration of the entrained inorganic species is more evident from consideration of the mean particle (polymer) separation distance $<r>$, which varies

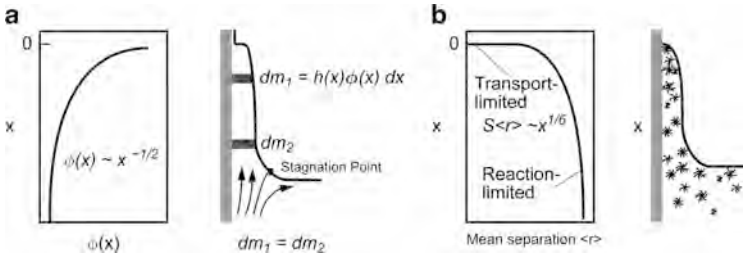

Fig. 10.5 (**a**) Fluid profile-concentration relationship for dip-coating. The conservation of non-volatile mass provides a relation between thickness profile $h(x)$ and the concentration $\phi(x)$ according to $h(x)\phi(x) = constant$. (**b**) Fluid profile mean separation relationship during dip-coating. From [15]

as the inverse cube root of ϕ, $<r> \sim x^{1/6}$ (Fig. 10.5b). This precipitous function implies that half the distance between particle (polymer) neighbors is traveled in the last 2 % of the deposition process, establishing a time scale of about 100 ms during which the condensed species are in close proximity. Several consequences of the short time scale of the film deposition processes may be anticipated:

- There is little time available for reacting species to "find" low energy configurations. Thus (for reactive systems) the dominant aggregative process responsible for network formation may change from reaction-limited (near the bath surface) to transport-limited near the drying line (Fig. 10.5b).
- For sols composed of repulsive particles, there is little time available for the particles to order as they are concentrated in the thinning film.
- There is little time available for condensation reactions to occur. Thus gelation may actually occur by a physical process, through the concentration dependence of the viscosity rather than a chemical process (In some systems this is evident by the fact that the deposited film is quickly re-solubilized when immersed in a solvent [17]).
- Since the thin physical or chemical gels are likely more weakly condensed, and hence, more compliant than bulk gels, they are more easily compacted first by evaporation and then by the capillary pressure exerted at the final stage of the deposition process (see Fig. 10.2). In such compliant materials the effects of capillary forces are enhanced, because greater shrinkage precedes the critical point, where the liquid-vapor interface first recedes into the gel (Fig. 10.2 inset), causing the pore size to be smaller and the maximum capillary pressure to be greater (see following discussion of drying).

10.3.2.2 Stages of Drying

Scherer [18] divides the drying of gels into two stages a constant rate period (CRP) and a falling rate period. During the constant rate period, mass transfer is limited by convection away from the gel surface, whereas during the falling rate period, mass

transfer is limited by the permeability of the gel. Extending these ideas to dip coating, it might be expected that a CRP would obtain throughout most of the deposition process, since the liquid-vapor interface remains located at the exterior surface of the thinning film except at the final stage of drying (see Fig. 10.2). As already mentioned above a constant evaporation rate implies a wedge-shaped film profile. This is not observed for pure fluids, nor is it observed for inorganic sols. For example, the film profile of a titanate sol prepared from titanium ethoxide hydrolyzed under acidic conditions in ethanol is described by $h(x) \sim x^{0.62}$ [5], which indicates that the evaporation rate increases as $x \rightarrow 0$, although not quite as rapidly as for pure ethanol ($h(x) \sim x^{0.5}$). Thus even for the deposition of inorganic sols, the film profile, and hence the concentration profile, are largely established by the dependence of the evaporation rate on the geometry of the depositing film Experiments performed on a variety of substrates, including metals, ceramics, and plastics all showed similar thickness profiles emphasizing that the evaporation rate, not the wetting characteristics are responsible for determining the profile shape [15]. For sols containing fluid mixtures of differing volatilities, the fluid composition changes with distance x, contributing to further changes in the evaporation rate. The critical point, where the liquid first recedes into the gel (see Fig. 10.2 inset) should mark the beginning of the falling rate period. Depending on the distribution of liquid in the pores, the drying rate is limited by flow or diffusion. For compliant molecular networks that are collapsed prior to the critical point, drying occurs by Fickian diffusion, if the temperature is above the glass transition temperature of the mixture [18]. The onset of a falling rate eriod near the drying line may account for the differences in the exponents that describe the shape of the pure fluid and the titanate sol film profiles.

10.3.2.3 Rheology

As the film becomes more concentrated in the condensed phase through evaporation, the rheological response of the liquid changes from Newtonian to shear thinning (aggregated systems) or thixotropic (ordered systems) and then to viscoelastic. Eventually gelation extends throughout the film and the material no longer yields, i.e. the film behaves as an elastic solid. It is at this final stage of the deposition process that the capillary pressure P_C created by tiny menisci as they recede into the gel, is maximized (see inset Fig. 10.2). The curvature of the menisci causes the liquid to be in tension and the network in compression. Generally the magnitude of the capillary pressure is estimated by the Laplace equation:

$$P_C = \frac{2\gamma_{LV}\cos(\theta)}{r_P} \tag{10.11}$$

where θ is the wetting angle and r_P is the pore size. For wetting pore fluids ($\cos\theta \rightarrow 1$), P_C could approach or possibly exceed 1,000 bar, because the pore size may be very small (less than 1.0 nm), i.e. approach molecular dimensions.

The capillary pressure thus represents a very strong driving force to densify the depositing film.

It is balance between this capillary pressure, which compresses the network, and the modulus of the network, which enables it to resist collapse, that establishes the final density and pore size of the film. Initially as the solvent evaporates, the gel is able to shrink. The volume fraction solids ϕ increases, causing the bulk modulus K to increase as a power law. In case of silica as an example, the following relationship is observed, valid for both wet and dry silica gels [18]:

$$K \sim \phi^{3.8} \tag{10.12}$$

At the same time the spacing between polymers (effective pore size) is decreasing, causing the maximum possible capillary pressure to increase approximately as:

$$\frac{1}{< r >} \sim \phi^{1/3} \tag{10.13}$$

Thus for silica films, the modulus is expected to increase more rapidly than the capillary pressure. When the modulus rises sufficiently to balance the capillary pressure, shrinkage stops, thereby establishing the pore size and density. Beyond this so-called critical point any further solvent loss creates porosity within the film. For precursor systems in which K exhibits a much weaker dependence on ϕ, for example as a consequence of organic modification or complexation of the metal centers with multidentate, non-hydrolyzable ligands, we might expect the network to be completely collapsed by the rising capillary pressure. However the rising viscosity accompanying solvent loss combined with the short time scale of the deposition process may represent a kinetic limitation to achieving a non-porous state. (It should also be pointed out that subsequent thermolysis and pyrolysis, respectively, of organic ligands will normally create porosity, even though the as-deposited film could be considered non-porous).

10.3.3 Drying Stress and Cracking

As the film dries, it shrinks in volume. Once the film is attached to the substrate and unable to shrink in that direction, the reduction in volume is accommodated completely by a reduction in thickness. When the film has solidified and stresses can no longer be relieved by flow, tensile stresses develop in the plane of the substrate. Croll [19] estimated the stress (σ) as:

$$\sigma = \left[\frac{E}{(1-\nu)}\right]\left[\frac{(f_S - f_r)}{3}\right] \tag{10.14}$$

where E is Young's modulus (Pa), ν is Poisson's ratio, f_S is the volume fraction solvent at the solidification point, and f_r is the volume fraction of residual solvent in the "dry" film.

The solidification point was defined for a polymer film as the concentration where the glass transition temperature has risen to the experimental temperature. Thus stress is proportional to Young's modulus and the difference between the solvent fraction at the solidification point and that of the dried coating. Scherer [2, 18] states that the stress in the film is very nearly equal to the tension in the liquid ($\sigma \approx P_C$). Despite such a large stress, it is commonly observed that cracking of films does not occur if the film thickness is below a certain critical thickness $h_c \approx 0.5$–1 μm [18]. For films that adhere well to the substrate, the critical thickness for crack propagation or the growth of pinholes is given by [20, 21]:

$$h_c = \left(\frac{K_{Ic}}{\sigma \Omega}\right)^2 \tag{10.15}$$

where K_{Ic} is the critical stress intensity or "fracture toughness" and Ω is a function that depends on the ratio of the elastic modulus of the film and substrate (for gel films $\Omega \approx 1$). For films thinner than h_c, the energy required to extend the crack is greater than the energy gained from relief of stresses near the crack, so cracking is not observed [18]. When the film thickness exceeds h_c, cracking occurs, and the crack patterns observed experimentally are qualitatively consistent with fractal patterns predicted by computer simulation [22]: Atkinson and Guppy [23] observed that the crack spacing increased with film thickness and attributed this behavior to a mechanism in which partial delamination accompanies crack propagation. Such delamination was observed directly by Garino [24] during the cracking of sol-gel silicate films. Based on Eqs. (10.14) and (10.15) above, strategies to avoid cracking include (a) increasing the fracture toughness (K_{Ic}) of the film, (b) reducing the modulus of the film, (c) reducing the volume fraction of solvent at the solidification point, and (d) reducing the film thickness. In organic polymer films, plasticizers are often added to reduce the stiffness of the film and thus avoid cracking [25]. For sol-gel systems, analogous results are obtained by organic modification of alkoxide precursors [26], chelation by multidentate ligands such as β-diketonates [27] or a reduction in the extent of hydrolysis of alkoxide precursors [24].

It should be noted that for particulate films Garino [28] observed that the maximum film thickness obtainable without cracks decreased linearly with a reduction in particle size. Since for unaggregated particulate films, the pore size scales with the particle size, this effect may be due to an increase in the stress caused by the capillary pressure ($\sigma \approx P_C$) and/or an increase in the volume fraction solvent at the solidification point resulting from the manner that the electrostatic double layer thickness (estimated by the Debye-Hückel screening length) varies with particle size [29].

10.3.4 Control of Microstructure

Basically the final film microstructure (of the as-deposited film) depends on a number of factors:

- the structure of the entrained inorganic species in the original sol (for example, size and fractal dimension)
- the reactivity of these species (for example, condensation or aggregation rates)
- the time scale of the deposition process (related to evaporation rate and film thickness)
- the magnitude of shear forces and capillary forces that accompany film deposition (related to surface tension of the solvent or carrier and surface tension gradients)

The most common means of controlling the film microstructure is through particle size. For unaggregated, monosized particulate sols, the pore size decreases and the surface area increases with decreasing particle size. Asymmetric, supported membranes have been prepared successfully from particulate sols for use in ultrafiltration [30]. As noted above difficulties arise when trying to prepare microporous membranes due to an increased tendency for cracking. Particulate sols may be intentionally aggregated prior to film formation to create very porous films [31] (e.g., volume porosity > 65 %). For electrostatically stabilized silica sols, a transition from random-close packing to ordered packing is observed with increasing substrate withdrawal rates (U_0) [31]. This may be due to a longer time scale of the deposition process (providing more time for ordering) or an increase in the shear rate accompanying deposition for higher U_0 [31]. A second strategy [2] for controlling porosity is based on the scaling of mass M_f and size r_f of a mass fractal object:

$$M_f \sim r_f^D \tag{10.16}$$

where D is the mass fractal dimension (in three dimensional space, $0 < D < 3$). Since density equals mass/volume, the density ρ_f of a mass fractal object varies in three dimensional space as $\rho_f \sim r_f^D / r_f^3$, and the porosity varies as $1/\rho_f \sim r_f^{(3-D)}$. Thus the porosity of a mass fractal object increases with its size. Providing that such fractals do not completely interpenetrate during film formation (i.e., they are mutually opaque, requiring $D < 1.5$ [2]), the porosity may be controlled by the size of the entrained fractal species prior to film formation. The efficacy of this approach is illustrated in ref. [31] where the refractive index, volume fraction porosity, pore size, and surface area of a multicomponent silicate film were shown to vary monotonically with aging time employed to grow the fractal species prior to film deposition. The extent of interpenetration of colliding fractals depends on their respective mass fractal dimensions and the condensation rate or "sticking probability" at points of intersection. A reduction of either D or the condensation rate increases the interpenetration and decreases the porosity [2, 31]. From

Eq. (10.16) and surrounding discussion, it follows that to generate porosity using this fractal scheme, r_f should be rather large, $1.5 \ll D \ll 3$, and the condensation rate should be high. Conversely dense films should be formed from small, unreactive precursors consistent with observations made on a variety of films prepared from chelated single and multicomponent alkoxide precursors [17]. The magnitude of the capillary pressure P_c should also be quite influential in determining microstructure. For bulk gels, elimination of surface tension by removal of the pore fluid above its critical point [32] results in highly porous aerogels. Deshpande and co-workers have recently shown that, for aprotic pore fluids, the surface area, pore volume, and pore size of bulk silica xerogels are all reduced monotonically by an increase in surface tension of the pore fluid [33]. Such studies are more difficult for films, since it is not possible to wash the coating sol, and distillation of solvents often leads to premature gelation. The most revealing studies are those comparing the effects of different hydrolysis ratios, $H_2O/M(OR)_n$, on film properties. Since the theoretical ratio for complete hydrolysis and condensation is $n/2$, greater ratios must produce "excess" water. As described above in mixed solvent systems, the least volatile component survives to the drying line and therefore dictates the magnitude of the capillary pressure. Fluorescence imaging experiments have shown that for alcohol/water mixtures containing more than about 10 volume % water, the composition of the fluid at the drying line is 100 % water [13]. It has been shown that as the "excess" water is increased from 0.5 to 6.0 volume %, the refractive index of silica films deposited by dipping increases from 1.342 to 1.431, corresponding to a reduction in porosity from 22 % to 7 % [34]. Further increases in the excess water content cause a reduction in refractive index (increase in porosity). Since water increases both the surface tension and the extent of condensation of the silicate matrix, this behavior reflects the competition between capillary pressure, which compacts the film, and aging, which stiffens the film increasing its resistance to compaction. In a similar dip-coating study, Warren and coworkers [35] observed that, for silica films annealed at 800 °C, the dielectric strength increased and the HF etch rate decreased as the hydrolysis ratio of the coating sol increased from 1 to 7.5. Further increases caused the reverse behavior. This implies that the effects of capillarity and aging also strongly influence the subsequent consolidation process. Finally it is anticipated that shear forces accompanying film formation could influence the microstructure. Although the withdrawal rates U_0 are often very low in dip-coating, it has been shown that surface tension gradient driven flows can cause high shear rates (10^4 s^{-1}) near the drying line [34]. Such shear rates might be partially responsible for the ordering of monosized particulate films [34].

10.3.5 Special Technical Approaches

In order to adjust the dip coating process to different substrates and substrate shapes the standard method has been technologically modified according to the specific

needs [36]. The major variations, which also found industrial interest, are presented briefly in the following paragraphs.

10.3.5.1 Drain Coating

The most self-evident modification is obtained, if not the sample is withdrawn from the coating solution, but the solution itself is removed by a constant draining rate. Although the simplest way of performing the draining can be achieved by gravity, in order to get a better control of the flow pulsation free liquid pumping is strongly recommended. This procedure called drain-coating leads physically to the same result as standard dip coating however requires less technical effort. On the other hand the substrate is in the more or less saturated solvent atmosphere of the vessel above the solution level for longer times compared to standard dip coating, which might lead to delayed drying and less hydrolysis/condensation reactions, i.e. film formation is hampered. In particular in case of sol-gel type precursor solutions the film formation is difficult to control and inhomogeneous coatings can result.

10.3.5.2 Angle-Dependent Dip Coating

In another modification the substrate withdrawal from the precursor solution is performed under a variable angle of inclination [37–39].

Different film thicknesses on both sides of the substrate with the thicker-coating on the upper side (Fig. 10.6a) are the outcome of this technique [40], whereupon the coating thickness is dependent on the angle between the substrate and the liquid surface. Thus a large number of thickness combinations on both sides can be realized by simple variation of the angle of inclination, the withdrawal speed and the solution concentration. Due to increasing border effects on the upper side, however, the operational range is limited to angles of inclination $<60^\circ$ and withdrawal speeds <10 mm/s [36]. A main field of interest of such unsymmetric coating systems is the preparation of optical interference filters [38, 39] because the number of coating steps can be reduced in most cases compared to other techniques.

10.3.5.3 Other Modifications

Further adaption may be applied to tailor the dip-coating technique to the corresponding applications [36]. Since naturally both sides of the substrate are coated but sometimes only coating on one side is tolerable the other side has to be protected from being coated. In order to accomplish this either two substrates e.g. in case of flat glass, could be joined at the borders with a chemically inert glue so that the interior is sealed or alternatively the side which should not be coated is protected by an adhesive foil. After coating the glue is removed by thermal processing resulting in two single side coated substrates, or the protective foil is

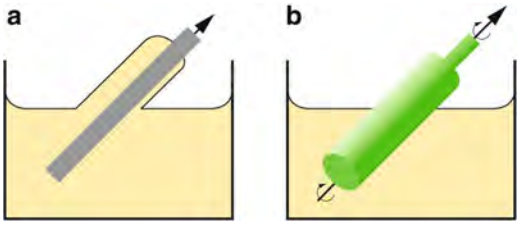

Fig. 10.6 Schematic of the technical setup for ADDC; (**a**) planar substrates and (**b**) rotationally symmetric bodies like bottles which are revolved during the withdrawal process

peeled of before high temperature curing of the as-deposited or dried film. Variations of the classical technique are also required for substrates with complex shapes such as bottles, threads or flange tubes, due to problems with thickness variations. In particular if deepened or leveled regions are coated the liquid film is too thick and thus may flake off. By revolving such rotationally symmetric substrates during the withdrawal process eventually combined with an angle like in angle-dependent dip coating (ADDC), a sufficient film leveling even on horizontal areas can be achieved due to the superposed centrifugal forces (Fig. 10.6b).

Even tubes and other cylindrical cavities can be coated from inside by special adaptions [41], which have to guarantee a forced laminar flow inside the tube in order to enable a complete solvent evaporation and hydrolysis of the film. Otherwise the drying of the liquid film is restricted in closed volumes due to saturation of evaporated solvents from the precursor solution and less hydrolysis. Puetz et al. [41] accomplished a suitable dip coating apparatus by an additional exhausting glass pipe (5 mm outer diameter) that was placed in the solution vessel and introduced from below into the tube with the internal end rising 5 mm above the solution (Fig. 10.7). After optimization optical ATO (antimony doped tin oxide) coatings were deposited inside tubes with inner diameters down to 11 mm exhibiting excellent thickness uniformity and an average roughness of less than 1 nm with a high reproducibility.

Beside these variations for batch conditions, continuous dip coating processes for endless flexible substrates like fibers and tapes are basically possible.

10.4 Evaporation Induced Self-Assembly

Among the modified dip coating methods the EISA process plays a prominent role since it allows not only for film formation but also for nanostructuring by using self-assembly principles of the nature. EISA is based on the fact that in dip coating film formation occurs through evaporation of solvents concentrating the system in non-volatile species (cp. Fig. 10.2), which leads to aggregation and gelation and hence can be also used to induce the formation of functional nanoscopic materials [42–46]. Thus precursor solutions containing amphiphilic molecules are utilized which become progressively concentrated through solvent evaporation thereby passing through structural and connectivity transitions taking place over seconds

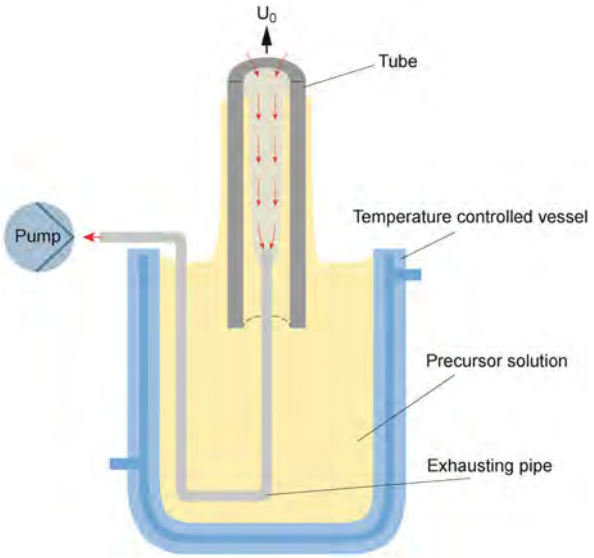

Fig. 10.7 Experimental set-up for the dip coating of tubes under forced flow conditions consisting of an internal exhausting pipe and a temperature controlled vessel. The external end of the exhausting pipe was connected to a diaphragm vacuum pump with an adjustable, constant flow of air of up to 210 l/h. The flow of air that is necessary to obtain homogeneous films depends on the withdrawal speed, on the inner diameter of the tube and also on the coating solution so that an optimisation is necessary. Modified after [41]

or fractions of a second. Figure 10.8 shows the several stages which can be stated [47].

As the solution becomes concentrated, the first transition that is important is the critical micelle concentration (CMC), in which the amphiphiles aggregate together into micellar or lamellar structures in a self-assembly process (Sect. 10.4.1). Upon further evaporation-induced crowding, these aggregates interact to form mesophases whose structures are determined—assuming there is time for equilibrium—by the phase behavior of the solvent(s) and surfactant. Finally, there is gelation of the sol-gel species, effectively locking into place the mesophase structure as evinced by its presence after complete evaporation of the solvents. It should be mentioned that during this drying environmental conditions, such as relative humidity, temperature and air flow have large impact on the microstructure development and hence have to be carefully controlled since sol–gel chemistry is highly sensitive to the water content and temperature.

In the following subsections some basic aspects of the EISA process and examples are described by means of silica in more detail.

10.4.1 Some Basics of Self-Assembly

A general definition of self-assembly is the spontaneous organization of materials through non-covalent interactions (hydrogen bonding, Van der Waals forces, electrostatic forces, π-π interactions, etc.) with no external intervention. Self-assembly typically employs asymmetric molecules that are pre-programmed to organize into well-defined supramolecular assemblies. Most common are amphiphilic surfactant

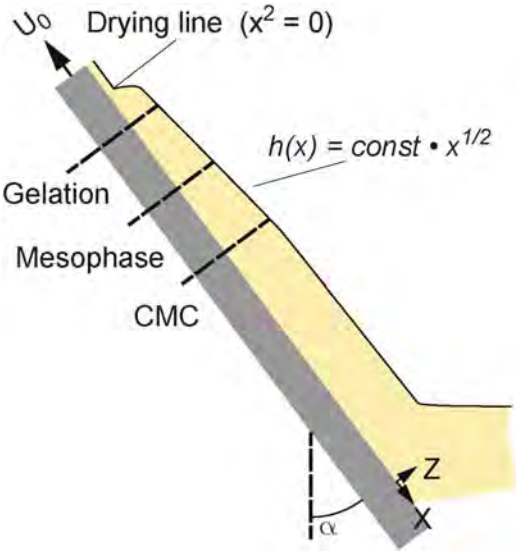

Fig. 10.8 Schematic representation of the different stages occurring during the drying of a liquid precursor film in dip coating. For generality withdrawal (U_0) is depicted at an angle α with respect to the vertical. The sequential transitions leading to the ordered porosity in thin films by the EISA process include the critical micelle concentration (CMC), in which surfactants aggregate into micelles, a transition from isotropic to a mesophase, and gelation of the sol to lock the mesophase structure in place. Adapted from [47]

molecules or polymers composed of hydrophobic and hydrophilic parts. In aqueous solution above the CMC, surfactants assemble into micelles, spherical or cylindrical structures that maintain the hydrophilic parts of the surfactant in contact with water while shielding the hydrophobic parts within the micellar interior (see Fig. 10.9).

Further increases in surfactant concentration result in the self-organization of micelles into periodic hexagonal, cubic, or lamellar mesophases (see insets in Fig. 10.9). Obviously such detergent mesophases do not themselves represent robust engineering materials suitable for nanotechnologies. However in 1992 Mobil researchers [48] discovered that surfactant self-assembly conducted in aqueous solutions of soluble silica species results in spontaneous coassembly of silica-surfactant mesophases. Surfactant removal creates periodic mesoporous solids, essentially silica fossils of the liquid-crystalline assembly. Over the last years, this pioneering work has been extended to produce a wide compositional range of mesoporous solids, and, using a variety of surfactants, the pore sizes have been varied in the approximate range, 1 nm to over 10 nm [49–53].

Despite excellent control of pore size, early mesoporous materials were made in the form of powders, precluding their use in thin film applications like membranes, low dielectric constant interlayers, and optical sensors. Stable, supported, mesoporous silica films were reported in 1996 [54–56].Typically, substrates were introduced into silica/surfactant/solvent systems used to prepare bulk hexagonal mesophases (initial surfactant concentrations $c_0 >$ CMC). Under these conditions, hexagonal silica-surfactant mesophases are nucleated on the substrate with pores oriented parallel to the substrate surface. Growth and coalescence over a period of hours to weeks resulted in continuous but macroscopically inhomogeneous films

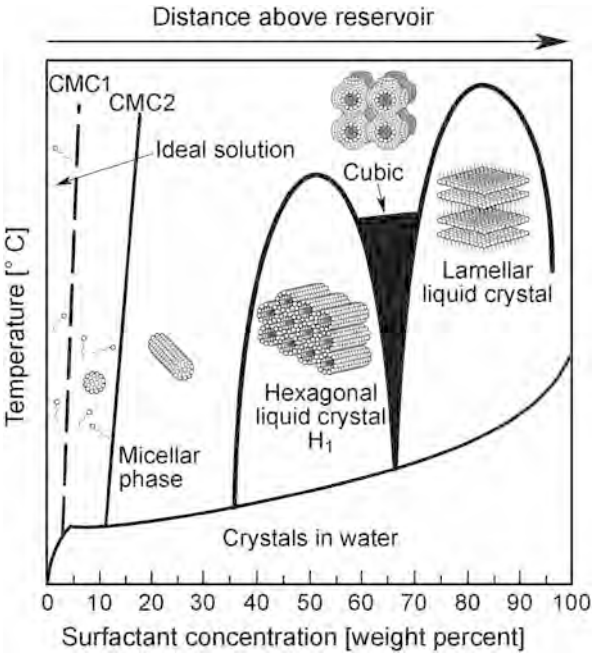

Fig. 10.9 Schematic phase diagram for cetyltrimethylammonium bromide (CTAB) in water. *Arrow* denotes evaporation-driven pathway during dip-coating, aerosol processing, etc. (Figure from [43] Brinker CJ, Lu YF, Sellinger A, Fan HY (1999) Evaporation-induced self-assembly: Nanostructures made easy. Adv Mater 11:579–585)

characterized by granular textures on micrometer-length scales. Göltner and Antonietti reviewed the advantages of direct templating by using liquid crystalline phases in the generalized preparation of mesoporous materials [57].

10.4.2 Details of the EISA Process

Consideration of Fig. 10.9 in the context of sol-gel dip coating suggests an alternative route to the formation of thin film mesophases. Beginning with a homogeneous solution of soluble silica and surfactant prepared in ethanol/water solvent with $c_0 << CMC$, preferential evaporation of ethanol concentrates the depositing film in water and nonvolatile surfactant and silica species (Fig. 10.10). The progressively increasing surfactant concentration drives self-assembly of silica-surfactant micelles and their further organization into various liquid crystalline mesophases [46, 58, 59]. Pre-existing, incipient silica-surfactant mesostructures (which exist at solid-liquid and liquid-vapor interfaces at $c < CMC$) serve to nucleate and orient the mesophase development [54, 59]. The result is rapid formation of thin film mesophases that are highly oriented with respect to the substrate surface. Through variation of the initial alcohol/water/surfactant molar ratio it is possible to follow different trajectories in composition space and to arrive at different final mesostructures. For example, using cetyltrimethylammonium bromide (CTAB), the formation of 1-D hexagonal, cubic, 3-D hexagonal and lamellar silica-surfactant

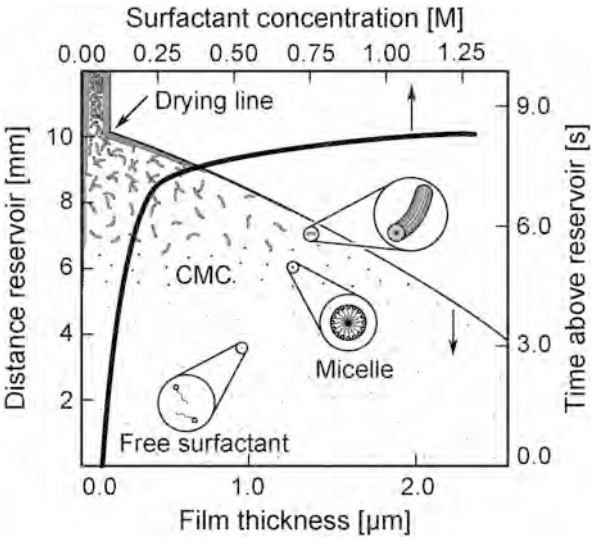

Fig. 10.10 Steady-state film thinning profile established during dip-coating of a complex fluid comprising soluble silica, surfactant, alcohol, and water. Initial surfactant concentration $c_0 << CMC$. Surfactant concentration increases with distance above the reservoir surface. Figure from [43]

mesophases was demonstrated [46, 56, 60]. Cubic thin film mesophases e.g. are essential for applications like membranes and sensors because they guarantee pore accessibility and through-film pore connectivity.

The dip coating scheme depicted in Fig. 10.10 represents a rapid (~10 s), dynamic self-assembly process conducted in a rather steep concentration gradient. Its steady, continuous nature promotes continuous accretion of micellar or perhaps liquid-crystalline species onto interfacially organized mesostructures. Large, liquid-crystalline domains grow progressively inward from the solid-liquid and liquid-vapor interfaces (with increasing distance above the reservoir surface, Fig. 10.10). Deposited films are optically transparent and completely featureless on the micrometer-length scale.

Essential to the ability to rapidly organize thin film mesophases is suppression of inorganic polymerization during the coating operation. For silicates this is achieved under acidic conditions at a hydronium ion concentration corresponding closely to the isoelectric point of colloidal silica ($[H_3O^+] \sim 0.01$) [2]. By first turning off siloxane condensation, an unimpeded proceeding of a cooperative silica-surfactant self-assembly is enabled, and the resulting as-deposited films exhibit liquid-crystalline (semi-solid) behavior. Thus the depositing film maintains a fluid state, even beyond the point where ethanol and water are largely evaporated. Subsequent aging, exposure to acid or base catalysts, or thermal treatment can solidify the silica skeleton, thereby locking in the desired mesostructure. Evidence for the liquid-crystalline nature of as-deposited films is several-fold:

1. There is dramatically less tensile stress developed during mesophase thin film deposition (5–10 MPa) compared to deposition of the same silica sol prepared without surfactants (~200 MPa). This virtual absence of drying stress suggests

that the film completely dries prior to solidification (i.e., as-deposited films are not solidified) [43].
2. Completely different mesophases (e.g., lamellar → cubic) can be obtained by transformation from the as-deposited mesophase films [46].
3. The as-deposited films exhibit self-healing tendencies, which enables the use of virtually any evaporation-driven process (spin-/dip coating, inkjet printing [61], or aerosol processing [44, 62] to create ordered nanostructures films, patterns [63], or particles. Even on complex shapes of (curved and flat) substrates (silicon wafers, glass slides, polymeric transparencies) self-assembled mesostructured silica can be prepared by a robot-directed aerosol printing process [62].

These combined liquid-crystalline characteristics make the EISA process robust and versatile. Due to this potential several other material systems have been successfully prepared meanwhile. For more details the reader is referred to some corresponding original works and references therein [64–68].

10.4.3 Extensions of EISA

In order to develop specific processes for different application purposes the EISA conditions have been modified and extended, respectively. Since an exhaustive description of all extensions leading to a bunch of periodically organized materials is beyond the scope of this chapter, two examples presented briefly in the following may serve to illustrate the possibilities.

10.4.3.1 Organic-Inorganic Nanocomposites

In standard EISA processing a calcination or solvent extraction step to remove the solvent follows in order to create inorganic mesoporous materials. Alternatively, EISA was used to create nanocomposite materials in which organic polymers or other organic components are uniformly incorporated within a periodic inorganic nanostructure [69]. The nanoscale organization of hard and soft materials is of interest for the development of optimized mechanical properties similar to those that occur in natural materials such as seashells, which are composed of alternating layers of crystalline calcium carbonate and biopolymers.

By using alcohol or tetrahydrofuran (THF) as a cosolvent, homogeneous, com-plex, multicomponent solutions can be prepared containing (in addition to the silicic acid precursors), organic monomers, cross-linkers, initiators, and cou-pling agents. During EISA, preferential evaporation of alcohol or THF concentrates the system in water. Rather than undergoing macroscopic phase separation, the hydro-phobic components are incorporated into micelles and mesophases. This allows hundreds of alternating silica/organic layers to be organized in a single step [69]. Subsequent in situ organic/inorganic polymerization results in a poly

(alkyl methacrylate)/silica nanocomposite with a covalently bonded polymer/silica interface. Such structures bear some relationship to seashells and other natural materials that are simultaneously hard, tough, and strong, i.e. mimicking biology.

An advancement of this nanocomposite self-assembly strategy is the use of polymerizable surfactants as structure-directing agents and monomers [70, 71]. The surfactant organizes the silicate nanostructure, as described earlier; subsequently, light, heat, or another treatment is used to polymerize the surfactant monomers, uniformly confined within a nanometer-scale "reaction vessel." As an advantage of this approach it is expected that the monomers to be uniformly organized within the surfactant mesophase, allowing potentially facile topochemical polymerization, where the topography of the monomeric diacetylenic (DA) assembly is preserved in the polymerized product, polydiactelyene (PDA). Using this approach Lu et al. [70] got blue PDA/silica nanocomposites after UV exposure, that exhibited thermo-, solvato- and mechanochromism, which are coloration effects occurring in response to thermal, mechanical, and chemical stimuli, respectively, to form the red fluorescent form. It should be noted that these properties are normally not observed in bulk PDA.

10.4.3.2 Nanocrystal Self-Assembly

The nanocomposite self-assembly strategy described above was expanded by employing other hydrophobic components in addition to hydrophobic organic monomers/molecules. Fan et al. investigated the self-assembly of hydrophobic nanocrystal (NC) mesophases within hydrophilic silica mesophases [72].

Typicall NC synthesis procedures use hydrophobic ligands (alkane thiols, trioctylphosphine oxide, etc.) to stabilize them from aggregation. Monosized NCs can be considered as moderate-sized hydrophobic molecules. It has been postulated that their incorporation as individual NCs in surfactant micelles would allow further self-assembly into ordered nanocrystalline mesophases, as anticipated from generic detergent phase diagrams. Rather than add hydrophobic NCs directly to isotropic surfactant/solvent/silica systems, as in polymer/silica self-assembly, a generic microemulsion procedure was developed to create water-soluble nanocrystal micelles. As represented schematically in Fig. 10.11a, a concentrated nanocrystal solution prepared in organic solvent (chloroform, hexane, etc.), is added to an aqueous solution of surfactant under vigorous stirring to create an oil-in-water microemulsion. Organic solvent evaporation then transfers the NCs into the aqueous phase by an interfacial process driven by the hydrophobic van der Waals interactions be-tween the primary alkanes of the NC stabilizing ligands and the secondary alkane of the surfactant. This results in thermodynamically defined interdigitated bilayer structures (Fig. 10.11b). Cationic, anionic, and non-ionic surfactants and phospholipids can all form NC micelles, allowing facile control of micelle surface charge and functionality. In addition, fluorescent semiconducting CdSe NCs (stabilized by trioctylphosphine oxide) have been formed into NC

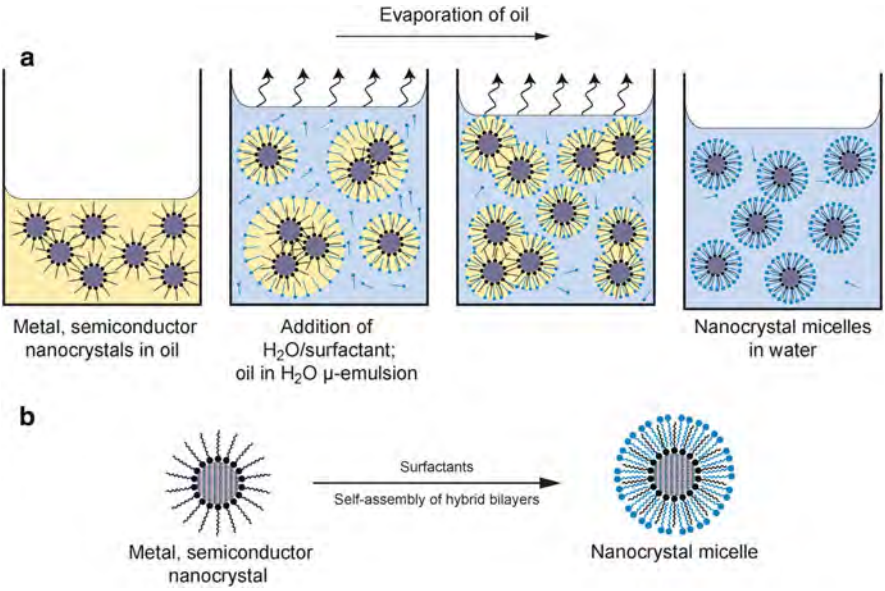

Fig. 10.11 Process scheme for the synthesis of water-soluble nanocrystal micelles. (**a**) The addition of oil containing nanocrystals (NCs) to a surfactant containing aqueous solution during vigorous stirring leads to the formation of an oil in H_2O microemulsion. Subsequent evaporation of oil transfers the NCs into the aqueous phase by an interfacial process driven by the hydrophobic van der Waals interactions between the primary alkane of the stabilizing ligand and the secondary alkane of the surfactant, resulting in thermodynamically defined interdigitated bilayer structures that encapsulate the NCs and make them water-soluble (**b**). Figure modified after [42]

micelles with maintenance of optical properties. This demonstrates the general nature and flexibility of this approach.

It has been discovered that in aqueous media, NC micelles organize hydrophilic components or precursors at the surfactant/water interface. This occurs through electrostatic and hydrogen-bonding interactions in a mechanism analogous to that of surfactant-directed self-assembly of silica/surfactant mesophases [73].

For example, addition of tetraethyl orthosilicate under **basic conditions** results in the formation of hydrophilic oligo-silicic acid species that organize with NC micelles to form a new type of ordered gold NC/silica mesophase. This nanocrystal mesophase has fcc symmetry (space group Fm3m) [72]. From a TEM investigation a fcc unit cell with a ≅10.2 nm and uniform spacing between NCs of ≅ 6 nm was deduced. This work [72] appears to be the first example of an ordered fcc nanocrystal array formed spontaneously by self-assembly in aqueous media rather than by solvent evaporation [74, 75]. Compared with other ordered NC arrays, the embedding silica matrix provides for greater chemical, mechanical, and thermal robustness. Furthermore, thermodynamically controlled self-assembly provides greater order and control of NC spacing, as compared with other connected nanocrystal systems such as those prepared by DNA hybridization [76, 77].

Thin film formation by means of typical deposition techniques like spin coating, etc. is allowed if **acidic conditions** designed to minimize the siloxane condensation rate are used. By suppressing siloxane condensation, and thereby gel formation, solvent evaporation accompanying coating induces self-assembly of NC micelles into fcc nano-crystal thin-film mesophases. This occurs in a manner similar to the evaporation-induced self-assembly of cubic or hexagonal silica/surfactant thin-film mesophases discussed earlier [46].

The formed ordered 3D NC arrays have been the subject of considerable interest, as they serve as model "artificial solids" with tunable electronic, magnetic, and optical properties stemming from single-electron charging and quantum confinement energies of individual NCs mediated by coupling interactions with neighboring NCs. Initial investigations of the charge transport properties of an ordered 3D nanocrystal array have been performed by means of planar metal–insulator–metal (MIM) devices, incorporating a Au NC/silica array as the insulator layer [72].

10.5 Summary

Although one of the oldest and apparently simplest film deposition methods, it is the dip coating process that serves as the link between the structure and properties of the liquid precursor sol and the microstructure of the corresponding deposited film. In spite of the fact that no universally valid model for the dip coating process has been obtained yet, the increasingly gained knowledge enables the controlled fabrication of various thin film microstructures from dense to ordered porous, nanocrystalline. Thereby film thickness is determined by the competition between surface tension (capillary force), gravity and viscosity. In many systems as a rule of thumb the faster the substrate is withdrawn, the thicker the film deposited. On the other hand however, thicker films may also be obtained if the "capillarity regime" is applied, where very low withdrawal speeds are used. Here solvent evaporation becomes faster than the movement of the drying line leading to a continuous feeding of the upper part of the meniscus and finally also to thicker films.

Since evaporation plays an important role in dip coating, the combination with suitable surfactants enables self-assembly of sol-gel precursor species leading to ordered nanoscopic thin films. Numerous variations of the generalized EISA process leading to ordered porous thin-film nanostructures have been carried out. Such porous materials are of interest for membranes, low-dielectric-constant (low-k) insulators, and dye sensitized solar cells. EISA can also be used to simultaneously organize hydrophilic and hydrophobic precursors into hybrid nanocomposites that are optically or chemically polymerizable, patternable, or adjustable. In some cases, even a pathway to materials is provided, that have no bulk nanostructured counter-parts (e.g., organic/inorganic nanocomposites). It is expected that further modifications of the theme of EISA processing will provide a convenient pathway to the formation of functional hierarchical devices, also in order to better emulate biology.

References

1. Geffcken W, Berger E (1939) Verfahren zur Änderung des Reflexionsvermögens optischer Gläser. Deutsches Reichspatent, assigned to Jenaer Glaswerk Schott & Gen., Jena 736 411
2. Brinker CJ, Scherer GW (1990) Sol-gel science. The physics and chemistry of sol–gel processing. Academic, San Diego
3. Baes CF, Mesmer RE (1976) The hydrolysis of cations. Wiley, New York
4. Livage J, Henry M, Sanchez C (1988) Sol-gel chemistry of transition metal oxides. Prog Solid State Chem 18:259–342
5. Brinker CJ, Hurd AJ, Frye GC, Schunk PR, Ashley CS (1991) Sol-gel thin film formation. J Ceram Soc Jpn 99:862–877
6. Scriven LE (1988) Physics and application of dip-coating and spin-coating. In: Brinker CJ, Clark DE, Ulrich DR (eds) Better ceramics through chemistry III, vol 121, Materials Research Society symposium proceedings. Materials Research Society, Pittsburgh, PA, pp 717–729
7. Landau LD, Levich VG (1942) Dragging of a liquid by a moving plate. Acta Phys Chim URSS 17:42–54
8. Grosso D (2011) How to exploit the full potential of the dip-coating process to better control film formation. J Mater Chem 21:17033–17038
9. Faustini M, Louis B, Albouy PA, Kuemmel M, Grosso D (2010) Preparation of sol-gel films by dip-coating in extreme conditions. J Phys Chem C 114:7637–7645
10. Lee CH, Lu YF, Shen AQ (2006) Evaporation induced self-assembly and rheology change during sol-gel coating. Phys Fluids 18:052105–052111
11. Brinker CJ, Hurd AJ, Schunk PR, Ashley CS (1992) Review of sol-gel thin film formation. J Non Cryst Solids 147–148:424–436
12. Hurd AJ, Brinker CJ (1988) Optical sol-gel coatings ellipsometry of film formation. J Phys France 49:1017–1025
13. Nishida F, Dunn B, Mckiernan JM, Zink JI, Brinker CJ, Hurd AJ (1994) In situ fluorescence imaging of sol-gel thin film deposition. J Sol-Gel Sci Technol 2:477–481
14. Nishida F, Mckiernan JM, Dunn B, Zink JI, Brinker CJ, Hurd AJ (1995) In situ fluorescence probing of the chemical changes during sol-gel thin film formation. J Am Ceram Soc 78:1640–1648
15. Hurd AJ (1994) Evaporation and surface tension effects in dip coating. In: Bergna HE (ed) The colloid chemistry of silica, vol 234, Advances in chemistry series. American Chemical Society, Washington, DC, pp 433–450, Chapter 21
16. Hurd AJ, Brinker CJ (1990) Sol-gel film formation by dip coating. In: Zelinski BJJ, Brinker CJ, Clark DE, Ulrich DR (eds) Better ceramics through chemistry IV, vol 180, Materials Research Society symposium proceedings. Materials Research Society, Pittsburgh, PA, pp 575–581
17. Schwartz RW, Voigt JA, Buchheit CD, Boyle TJ (1994) Densification and crystallization of zirconia thin films prepared by sol-gel processing. Ceram Trans 43:145–163
18. Scherer GW (1992) Recent progress in drying of gels. J Non-Cryst Solids 147–148:363–374
19. Croll SG (1979) The origin of residual internal stress in solvent-cast thermoplastic coatings. J Appl Polymer Sci 23:847–853
20. Evans AJ, Dory MD, Hu MS (1988) The cracking and decohesion of thin films. J Mater Res 3:1043–1054
21. Thouless MD (1988) Decohesion of films with axisymetric geometrics. Acta Metall 36:3131–3139
22. Meakin P (1991) Models for materials failure and deformation. Science 252:226–229
23. Atkinson A, Guppy RM (1991) Mechanical stability of sol-gel films. J Mater Sci 26:3869–3875
24. Garino TJ (1990) The cracking of sol-gel thin films during drying. In: Zelinski BJJ, Brinker CJ, Clark DE, Ulrich DR (eds) Better ceramics through chemistry IV, vol 180, Materials Research Society symposium proceedings. Materials Research Society, Pittsburgh, PA, pp 497–502

25. Cohen ED, Gutoff EB, Lightfoot EJ (1990) A primer on forming coatings. Chem Eng Prog 86:30–36
26. Takahashi Y, Matsuoka Y, Yamaguchi K, Matsuki M, Kobayashi K (1990) Dip coating of PT, PZ, and PZT films using an alkoxide-diethanolamine method. J Mater Sci 25:3960–3964
27. Schmidt H, Rinn G, Nass R, Sporn D (1988) Film formation by inorganic-organic sol-gel synthesis. In: Brinker CJ, Clark DE, Ulrich DR (eds) Better ceramics through chemistry III, vol 121, Materials Research Society symposium proceedings. Materials Research Society, Pittsburgh, PA, pp 743–752
28. Garino TJ (1988) PhD Thesis, MIT
29. Brinker CJ, Scherer GW (1990) Sol-gel science. The physics and chemistry of sol–gel processing. Academic, San Diego, pp 235–301, Chapter 4
30. Bhave RR (ed) (1991) Inorganic membranes. Van Nostrand Reinhold, New York (many examples are provided)
31. Brinker CJ, Hurd AJ, Frye GC, Ward KJ, Ashley CS (1990) Sol-gel thin film formation. J Non-Cryst Solids 121:294–308
32. Brinker CJ, Scherer GW (1990) Sol-gel science. The physics and chemistry of sol–gel processing. Academic, San Diego, pp 493–505, Chapter 8
33. Deshpande R, Hua D-W, Smith DM, Brinker CJ (1992) Pore structure evolution in silica gels during aging and drying: 3. Effects of surface tension. J Non-Cryst Solids 144:32–43
34. Brinker CJ, Frye GC, Hurd AJ, Ashley CS (1991) Fundamentals of sol-gel dip coating. Thin Solid Films 201:97–108
35. Warren WL, Lenahan PM, Brinker CJ, Shaffer GR, Ashley CS, Reed ST (1990) Sol-gel thin film electronic properties. In: Zelinski BJJ, Brinker CJ, Clark DE, Ulrich DR (eds) Better ceramics through chemistry IV, vol 180, Materials Research Society symposium proceedings. Materials Research Society, Pittsburgh, PA, pp 413–419
36. Puetz J, Aegerter MA (2004) Dip coating technique. In: Aegerter MA, Mennig M (eds) Sol-gel technologies for glass producers and users, 1st edn. Kluwer, Boston
37. Schröder H (1969) Oxide layers deposited from organic solutions. In: Hass G, Thun RE (eds) Physics of thin films, vol 5. Academic, London, pp 87–141
38. Arfsten NI, Eberle A, Otto J, Reich A (1997) Investigations on the angle-dependent dip coating technique (ADDC) for the production of optical filters. J Sol-Gel Sci Technol 8:1099–1104
39. Mennig M, Oliveira PW, Frantzen A, Schmidt H (1999) Multilayer NIR reflective coatings on transparent plastic substrates from photopolymerizable nanoparticulate sols. Thin Solid Films 351:225–229
40. Tallmadge IA (1971) A theory of entrainment for angular withdrawal of flat supports. AIChE J 17:243–246
41. Puetz J, Chalvet FN, Aegerter MA (2003) Wet chemical deposition of transparent conducting coatings in glass tubes. Thin Solid Films 442:53–59
42. Brinker CJ (2004) Evaporation-induced self-assembly: functional nanostructures made easy. MRS Bull 29:631–639
43. Brinker CJ, Lu YF, Sellinger A, Fan HY (1999) Evaporation-induced self-assembly: nanostructures made easy. Adv Mater 11:579–585
44. Lu YF, Fan HY, Stump A, Ward TL, Rieker T, Brinker CJ (1999) Aerosol-assisted self-assembly of mesostructured spherical nanoparticles. Nature 398:223–226
45. Lu YF, Cao GZ, Kale RP, Prabakar S, Lopez GP, Brinker CJ (1999) Microporous silica prepared by organic templating: relationship between the molecular template and pore structure. Chem Mater 11:1223–1229
46. Lu Y, Ganguli R, Drewien CA, Anderson MT, Brinker CJ, Gong W, Guo Y, Soyez H, Dunn B, Huang MH, Zink JI (1997) Continuous formation of supported cubic and hexagonal mesoporous films by sol–gel dip-coating. Nature 389:364–368
47. Hurd AJ, Steinberg L (2001) The physics of evaporation-induced assembly of sol-gel materials. Granul Matter 3:19–21

48. Kresge C, Leonowicz M, Roth W, Vartuli C, Beck J (1992) Ordered mesoporous molecular sieves synthesized by a liquid-crystal template mechanism. Nature 359:710–712
49. Huo Q, Margolese D, Ciesla U, Feng P, Gier TG, Sieger P, Leon R, Petroff PM, Schuth F, Stucky G (1994) Generalized synthesis of periodic surfactant/inorganic composite materials. Nature 368:317–321
50. Firouzi A, Kumar D, Bull LM, Besier T, Sieger P, Huo Q, Walker SA, Zasadzinski JA, Glinka C, Nicol J, Margolese D, Stucky GD, Chmelka BF (1995) Cooperative organization of inorganic-surfactant and biomimetic assemblies. Science 267:1138–1143
51. Tanev PT, Pinnavaia TJ (1995) A neutral templating route to mesoporous molecular sieves. Science 267:865–867
52. Antonelli DM, Ying JY (1995) Synthesis of hexagonally packed mesoporous TiO_2 by a modified sol–gel method. Angew Chem Int Ed Engl 34:2014–2017
53. Zhao D, Feng J, Huo Q, Nelosh N, Fredrickson G, Chmelka B, Stucky GD (1998) Triblock copolymer syntheses of mesoporous silica with periodic 50 to 300 angstrom pores. Science 279:548–552
54. Aksay I, Trau M, Manne S, Honma I, Yao N, Zhou L, Fenter P, Eisenberger P, Gruner S (1996) Biomimetic pathways for assembling inorganic thin films. Science 273:892–898
55. Yang H, Kuperman A, Coombs N, Mamiche-Afara S, Ozin GA (1996) Synthesis of oriented films of mesoporous silica on mica. Nature 379:703–705
56. Ogawa M (1996) A simple sol–gel route for the preparation of silica–surfactant mesostructured materials. Chem Commun 1996:1149–1150
57. Göltner CG, Antonietti M (1997) Mesoporous materials by templating of liquid crystalline phases. Adv Mater 9:431–436
58. Bruinsma PJ, Kim AY, Liu J, Baskaran S (1997) Mesoporous silica synthesized by solvent evaporation: spun fibers and spray-dried hollow spheres. Chem Mater 9:2507–2512
59. Ogawa M (1994) Formation of novel oriented transparent films of layered silica-surfactant nanocomposites. J Am Chem Soc 116:7941–7942
60. Yang H, Coombs N, Sokolov I, Ozin GA (1996) Free-standing and oriented mesoporous silica films grown at the air–water interface. Nature 381:589–592
61. Fan H, Lu Y, Stump A, Reed ST, Baer T, Schunk R, Perez-Luna V, López GP, Brinker CJ (2000) Rapid prototyping of patterned functional nanostructures. Nature 405:56–60
62. Pang J, Stuecker JN, Jiang Y, Bhakta AJ, Branson ED, Li P, Cesarano J III, Sutton D, Calvert P, Brinker CJ (2008) Directed aerosol writing of ordered silica nanostructures on arbitrary surfaces with self-assembling inks. Small 4:982–989
63. Doshi DA, Huesing NK, Lu M, Fan H, Lu Y, Simmons-Potter K, Potter BG Jr, Hurd AJ, Brinker CJ (2000) Optically defined multifunctional patterning of photosensitive thin-film silica mesophases. Science 290:107–111
64. Brezesinski K, Haetge J, Wang J, Mascotto S, Reitz C, Rein A, Tolbert SH, Perlich J, Dunn B, Brezesinski T (2011) Ordered mesoporous α-Fe_2O_3 (Hematite) thin-film electrodes for application in high rate rechargeable lithium batteries. Small 7:407–414
65. Kuemmel M, Grosso D, Boissière C, Smarsly B, Brezesinski T, Albouy PA, Amenitsch H, Sanchez C (2005) Thermally stable nanocrystalline γ-alumina layers with highly ordered 3D mesoporosity. Angew Chem Int Ed 44:4589–4592
66. Smarsly B, Grosso D, Brezesinski T, Pinna N, Boissieère C, Antonietti M, Sanchez C (2004) Highly crystalline cubic mesoporous TiO_2 with 10-nm pore diameter made with a new block copolymer template. Chem Mater 16:2948–2952
67. Grosso D, Boissière C, Smarsly B, Brezesinski T, Pinna N, Albouy PA, Amenitsch H, Antonietti M, Sanchez C (2004) Periodically ordered nanoscale islands and mesoporous films composed of nanocrystalline multimetallic oxides. Nat Mater 3:787–792
68. Grosso D, Cagnol F, Soler-Illia GJAA, Crepaldi EL, Amenitsch H, Brunet-Bruneau A, Bourgeois A, Sanchez C (2004) Fundamentals of mesostructuring through evaporation-induced self-assembly. Adv Funct Mater 14:309–322

69. Sellinger A, Weiss PM, Nguyen A, Lu Y, Assink RA, Gong W, Brinker CJ (1998) Continuous self-assembly of organic–inorganic nanocomposite coatings that mimic nacre. Nature 394:256–260
70. Lu Y, Yang Y, Sellinger A, Lu M, Huang J, Fan H, Haddad R, Lopez G, Burns Alan R, Sasaki DY, Shelnutt J, Brinker CJ (2001) Self-assembly of mesoscopically ordered chromatic polydiacetylene/silica nanocomposites. Nature 410:913–917
71. Yang Y, Lu Y, Lu M, Huang J, Haddad R, Xomeritakis G, Liu N, Malanoski AP, Sturmayr D, Fan H, Sasaki DJ, Assink RA, Shelnutt JA, van Swol F, Lopez GP, Burns AR, Brinker CJ (2003) Functional nanocomposites prepared by self-assembly and polymerization of diacetylene surfactants and silicic acid. J Am Chem Soc 125:1269–1277
72. Fan H, Yang K, Boye DM, Sigmon T, Malloy KJ, Xu H, Brinker CJ (2004) Self-assembly of ordered, robust, three-dimensional gold/silica nanocrystal arrays. Science 304:567–571
73. Beck JS, Vartuli JC, Roth WJ, Leonowicz ME, Kresge CT, Schmitt KD, Chu CTW, Olson DH, Sheppard EW, McCullen SB, Higgins JB, Schlenker JL (1992) A new family of mesoporous molecular sieves prepared with liquid crystal templates. J Am Chem Soc 114:10834–10843
74. Murray CB, Kagan CR, Bawendi MG (1995) Self-organization of CdSe nanocrystallites into three-dimensional quantum dot superlattices. Science 270:1335–1338
75. Sun SH, Murray CB, Weller D, Folks L, Moser A (2000) Nanocrystal superlattices monodisperse FePt nanoparticles and ferromagnetic FePt. Science 287:1989–1992
76. Mirkin CA, Letsinger RL, Mucic RC, Storhoff JJ (1996) A DNA-based method for rationally assembling nanoparticles into macroscopic materials. Nature 382:607–609
77. Alivisatos AP, Johnsson KP, Peng XG, Wilson TE, Loweth CJ, Bruchez MP, Schultz PG (1996) Organization of 'nanocrystal molecules' using DNA. Nature 382:609–611